Electromagnetic Thermal Energy Transfer in Nanoparticle Assemblies Below Diffraction Limit

Anil Yuksel
Department of Mechanical Engineering,
The University of Texas at Austin,
Austin, TX 78712
e-mail: anil.yuksel@utexas.edu

Edward T. Yu
Microelectronics Research Center,
Department of Electrical and Computer Engineering,
The University of Texas at Austin,
Austin, TX 78712
e-mail: ety@ece.utexas.edu

Michael Cullinan
Department of Mechanical Engineering,
The University of Texas at Austin,
Austin, TX 78712
e-mail: michael.cullinan@austin.utexas.edu

Jayathi Murthy
Henry Samueli School of Engineering and Applied Science,
University of California, Los Angeles,
Los Angeles, CA 90095
e-mail: jmurthy@ucla.edu

Fabrication of micro- and nanoscale electronic components has become increasingly demanding due to device and interconnect scaling combined with advanced packaging and assembly for electronic, aerospace, and medical applications. Recent advances in additive manufacturing have made it possible to fabricate microscale, 3D interconnect structures but heat transfer during the fabrication process is one of the most important phenomena influencing the reliable manufacturing of these interconnect structures. In this study, optical absorption and scattering by three-dimensional (3D) nanoparticle packings are investigated to gain insight into micro/nano heat transport within the nanoparticles. Because drying of colloidal solutions creates different configurations of nanoparticles, the plasmonic coupling in three different copper nanoparticle packing configurations was investigated: simple cubic (SC), face-centered cubic (FCC), and hexagonal close packing (HCP). Single-scatter albedo (ω) was analyzed as a function of nanoparticle size, packing density, and configuration to assess effect for thermo-optical properties and plasmonic coupling of the Cu nanoparticles within the nanoparticle packings. This analysis provides insight into plasmonically enhanced absorption in copper nanoparticle particles and its consequences for laser heating of nanoparticle assemblies.
[DOI: 10.1115/1.4047631]

Keywords: nanotechnology, surface plasmon polaritons, near-field energy enhancement, heat transfer enhancement, micro/nanoscale heat transfer, radiative heat transfer, thermal systems

1 Introduction

Thermal energy transport in nanoparticle packings has been of interest recently due to various potential micro/nano applications [1,2]. At subwavelength length scales, the physics of the energy transport depends mainly on the thermo-optical response from the nanostructures [3,4]. This dependence arises from the oscillations of the conduction electrons which result in plasmon generation in metal nanoparticles [5]. The generation of the plasmonic resonances is highly sensitive to the particle size, the material, the dielectric medium, the ordering of the particles, and the light source properties [6]. Certain combinations of particle configuration, size, and the wavelength of the incoming source create resonance conditions which lead to very strong local electromagnetic energy enhancements. Indeed, thermal transport of this energy in plasmon waveguides relies on near-field coupling between the particles, and such enhanced local fields can result in nonlinear thermo-optical responses from the nanoparticle packings [7–9]. However, the nonlinear responses of nanoparticle packings are not yet well understood [10–12]. One of the main reasons for this lack of understanding is that nanoparticles start to agglomerate due to the van der Waals attraction when organized into a powder bed [13]. There has been some analysis on different configurations such as periodic arrays of nanoparticles in two-dimensional (2D) and few particle three-dimensional (3D) configurations to demonstrate the electromagnetic coupling between the nanoparticles [14–16]. Well-ordered 2D configuration analysis has been performed in pursuit of various micro/nano applications; however, many particle and disordered 3D nanoparticle configurations have not yet been investigated [17]. Indeed, different nanoparticle configurations with different nanoparticle sizes create major challenges for micro/nano electronics [4,18]. Size effects result in nonlocal and nonlinear heat transport or heat flux dissipation based on electron scattering, surface scattering specularity, and grain boundary effects. Also, thermal boundary conductance leads to a finite temperature discontinuity at the interface of the metallic nanoparticles. This is mainly due to the electron scattering at the interface of the metal nanoparticles that changes the electronic and vibrational properties. High thermal conductance is important for high heat dissipation, and it is governed mainly by electron scattering at the metal–metal interface. Due to the various probabilities of the electron scattering within the close-packed metal nanoparticle packings, the interparticle spacing and configuration guide the plasmon waveguides, group velocity, and dispersion relation for the thermal energy transport [18].

In this paper, characteristics of optical electromagnetic energy propagation in different copper (Cu) nanoparticle configurations and different particle sizes are determined and analyzed using finite-difference frequency-domain simulations. The thermo-optical properties, the resistive heating, and single-scatter albedo (ω) are analyzed within simple cubic (SC), hexagonal close packing (HCP), and face-centered cubic (FCC) nanoparticle packings with 25 nm, 50 nm and 75 nm radius, monodispersed Cu nanoparticles under a 532-nm transverse magnetic (TM) polarized laser/light source. The 532-nm wavelength light source was chosen because it is widely preferred for metal nanoparticle-laser-related industrial applications.

2 Modeling Analysis

Laser interaction with nanoparticle packing results in various different regimes on the substrate due to thermal transport such as heat affected zone, sintered nanoparticle packing area, and the unsintered

Manuscript received October 20, 2019; final manuscript received March 25, 2020; published online August 5, 2020. Assoc. Editor: Aaron P. Wemhoff.

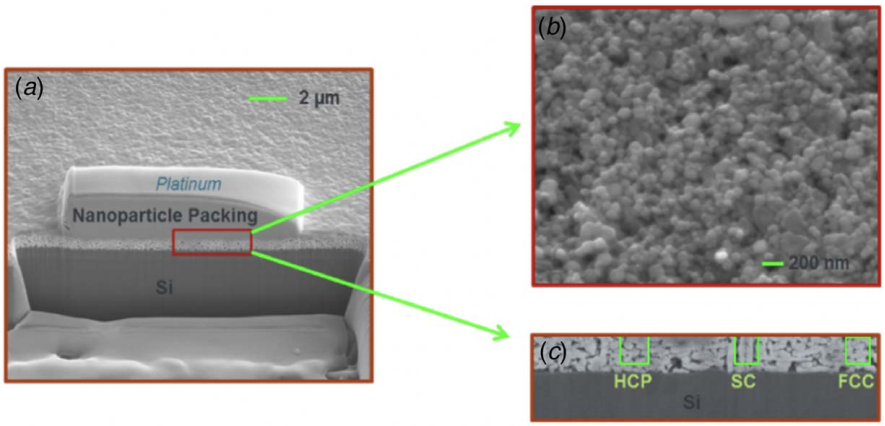

Fig. 1 Cu nanoparticle packing on a silicon wafer supported by platinum and FIB cross-sectional morphology imaged using scanning electron microscope (SEM): (*a*) low-magnification surface view, (*b*) SEM view, and (*c*) FIB cross-sectional morphology showing the HCP, SC, and FCC configurations

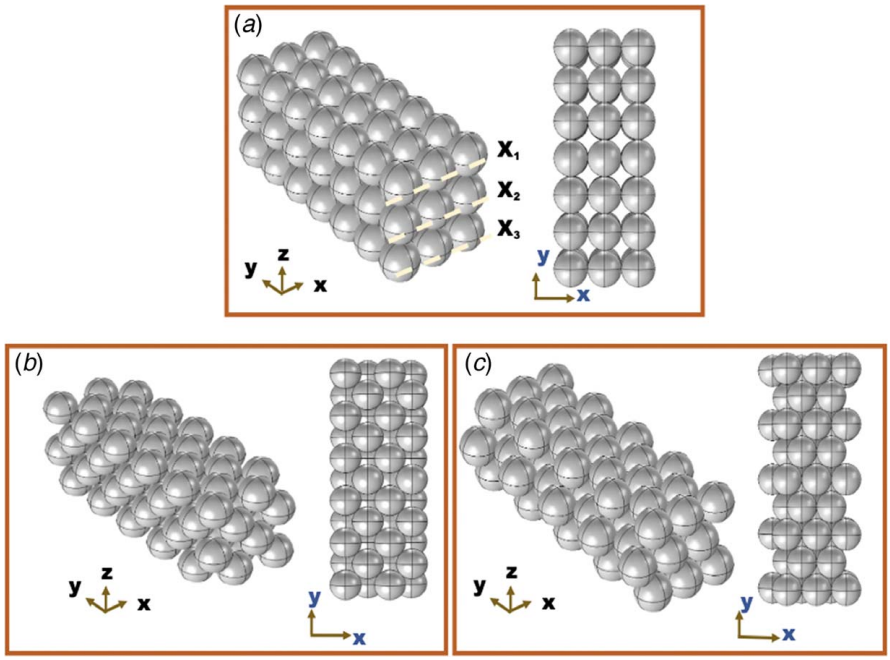

Fig. 2 Nanoparticle packing configurations: (*a*) SC, (*b*) FCC, and (*c*) HCP

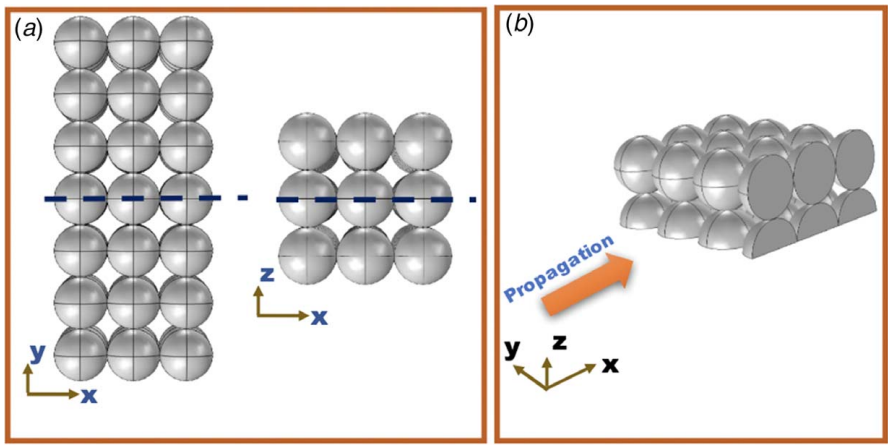

Fig. 3 Sample SC nanoparticle packing modeling approach: (*a*) symmetry planes for SC nanoparticle packing and (*b*) simulated geometry

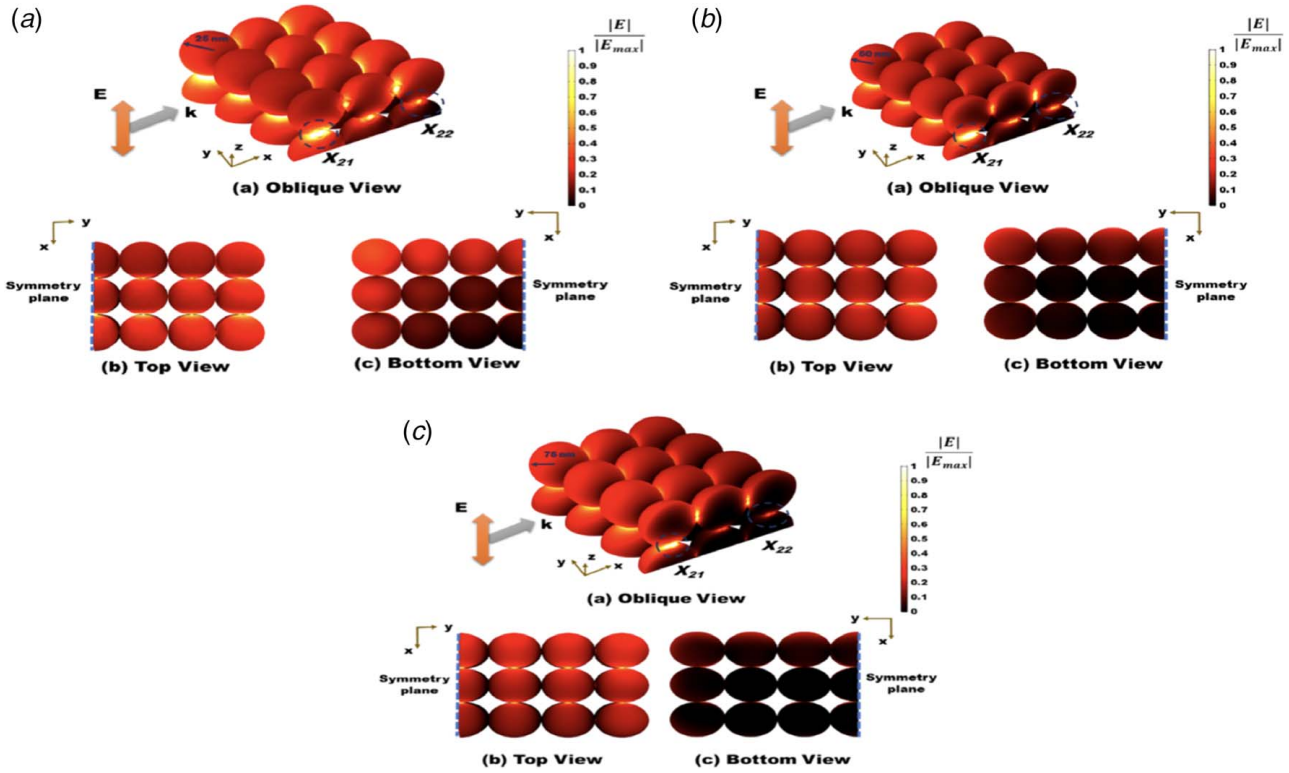

Fig. 4 Electric field distribution with $\lambda = 532$ nm, TM polarized light with varying radius for SC configuration: (*a*) 25-nm radius, (*b*) 50-nm radius and (c) 75-nm radius

nanoparticle clusters. Thus, laser sintering process is mainly driven by the heat transport between the nanoparticles which are placed onto a substrate. In this study, we use the three-dimensional (3D) finite-difference frequency-domain method to obtain the electromagnetic field distribution around the metallic nanoparticles by solving Maxwell's equations. The complex permittivity of the Cu nanoparticle is used from Johnson and Christy [19].

Figure 1 shows a representative copper nanoparticle packing on a silicon wafer. After the drying of the colloidal solution used to deposit the nanoparticles on the surface of the substrate, we observed some configurations that look like SC, HCP, and FCC under focused ion beam (FIB), which is also the motivation for modeling the nanoparticle packing configurations in this study. Indeed, particle distribution does not fully obey any one of the specific configurations along the cross-sectional view due to the high agglomeration resulting from van der Waals attractions between the copper nanoparticles [13]. The average diameter of the particles is measured to be about 100 nm with a standard deviation of about 40 nm.

Metallic nanoparticles exhibit different plasmonic effects at different gap distances as well as when placed at different locations with respect to each other. Therefore, we analyzed three different

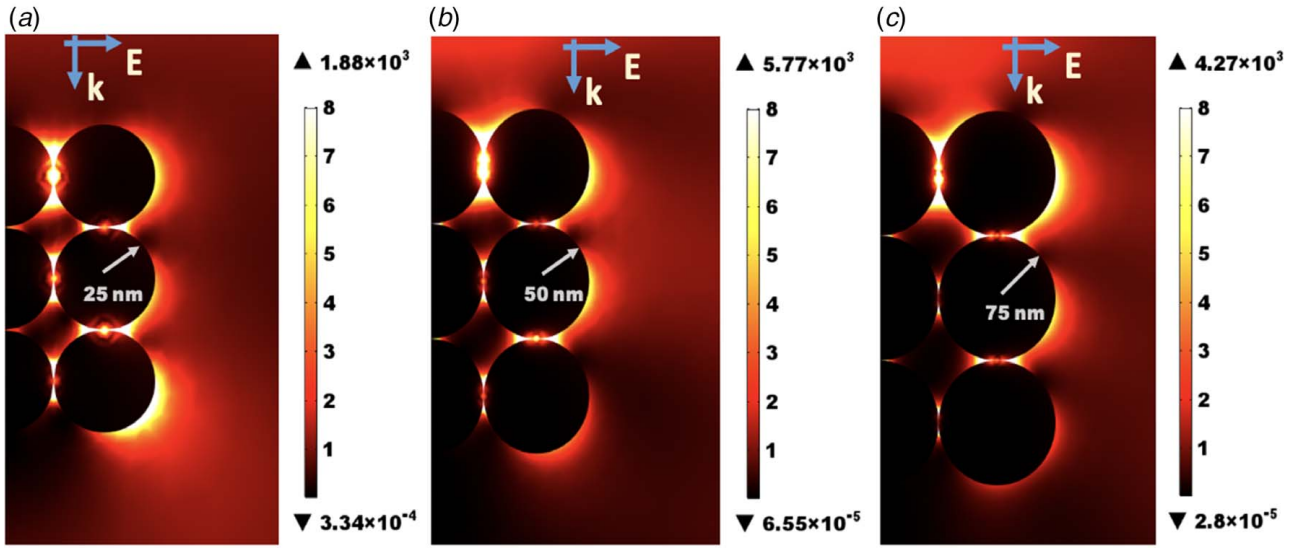

Fig. 5 Electric field intensity ($|I/I_0|$) with $\lambda = 532$ nm, TM polarized light with varying radius for SC configuration at X_{21} and X_{22} cross section (x−z plane at $y = 0$)

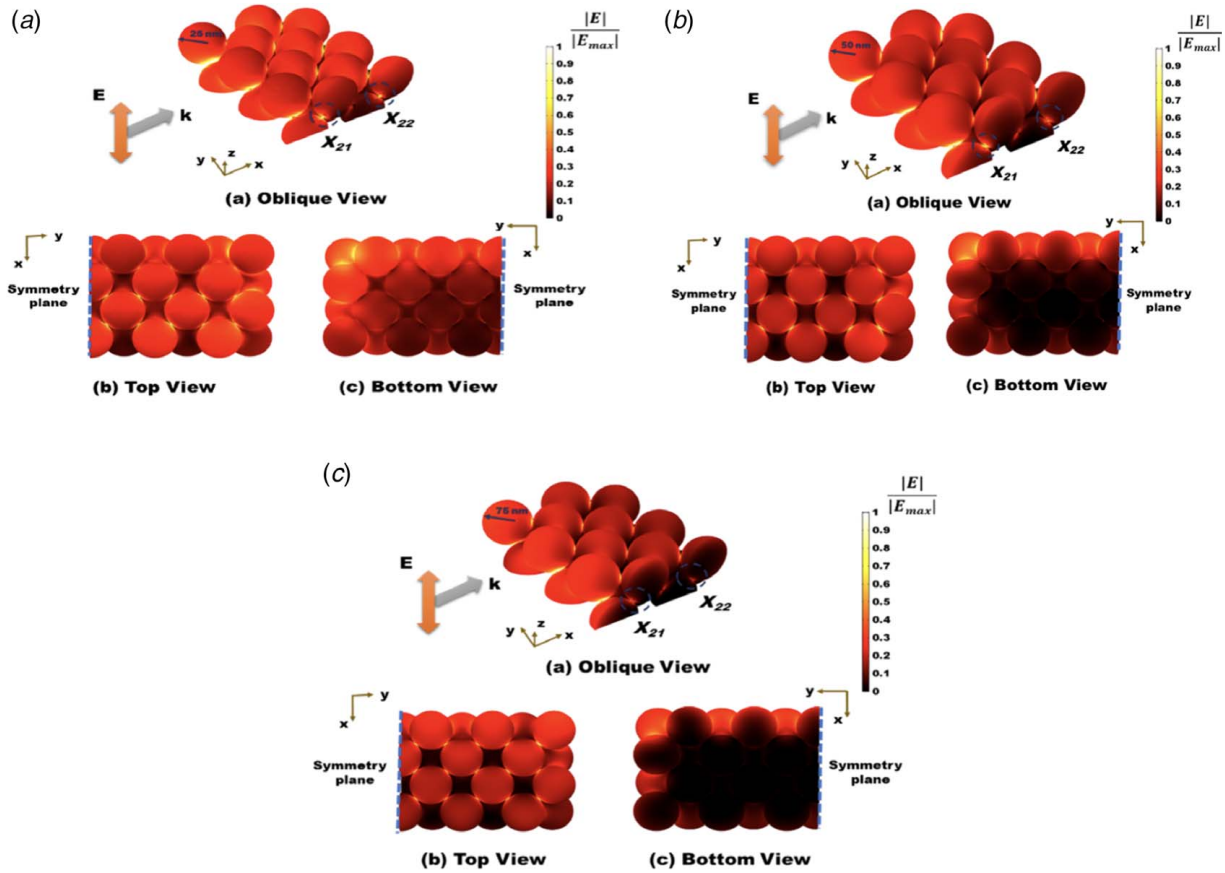

Fig. 6 Electric field distribution with $\lambda = 532$ nm, TM polarized light with varying radius for FCC configuration: (*a*) 25-nm radius, (*b*) 50-nm radius, and (c) 75-nm radius

particle packing configurations (SC, FCC, and HCP) with the effective layer thickness observed from Fig. 1 to understand the thermo-optical properties of the nanoparticle packings. These packing configurations are shown in Fig. 2.

In this study, we use 532-nm TM polarized (z-polarized) plane wave illumination with $E_0 = 1$ V/m, propagating in the x direction as shown in Fig. 3(*b*) for all the analyzed particle configurations. Nanoparticles with radii of 25 nm, 50 nm, and 75 nm are used which is motivated by the fact that copper nanoparticle's absorption and scattering cross sections are equal for about 65-nm radius single spherical Cu nanoparticle under 532-nm light illumination from the calculation. Also, symmetry is utilized to reduce the computational

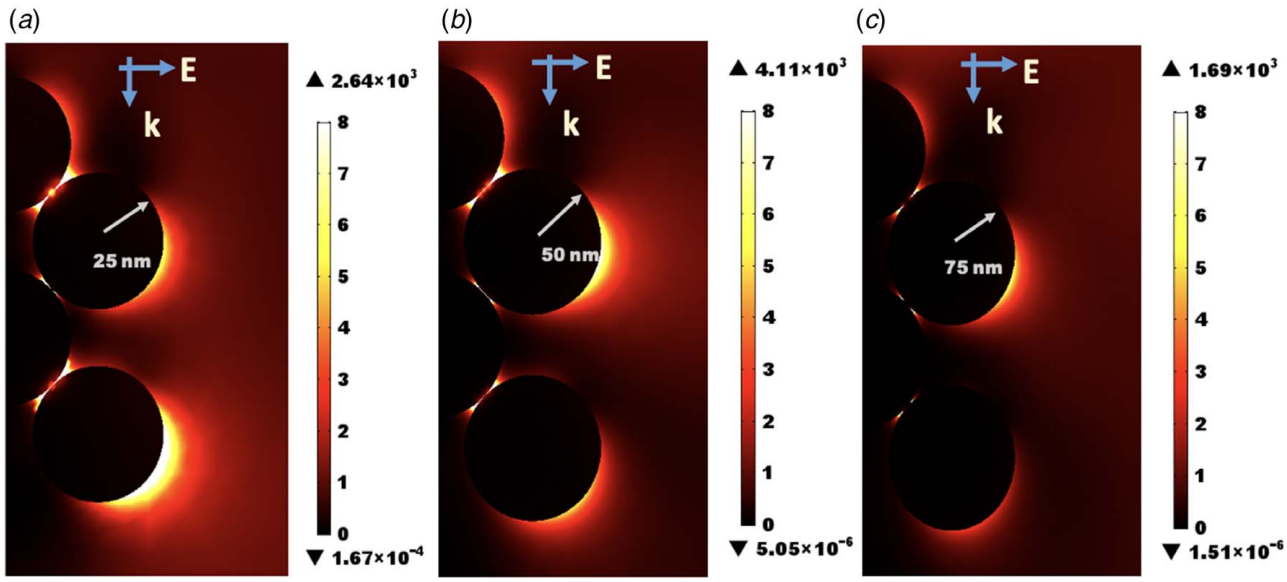

Fig. 7 Electric field intensity ($|I/I_0|$) with $\lambda = 532$ nm, TM polarized light with varying radius for FCC configuration at X_{21} and X_{22} cross section (x–z plane at $y = 0$)

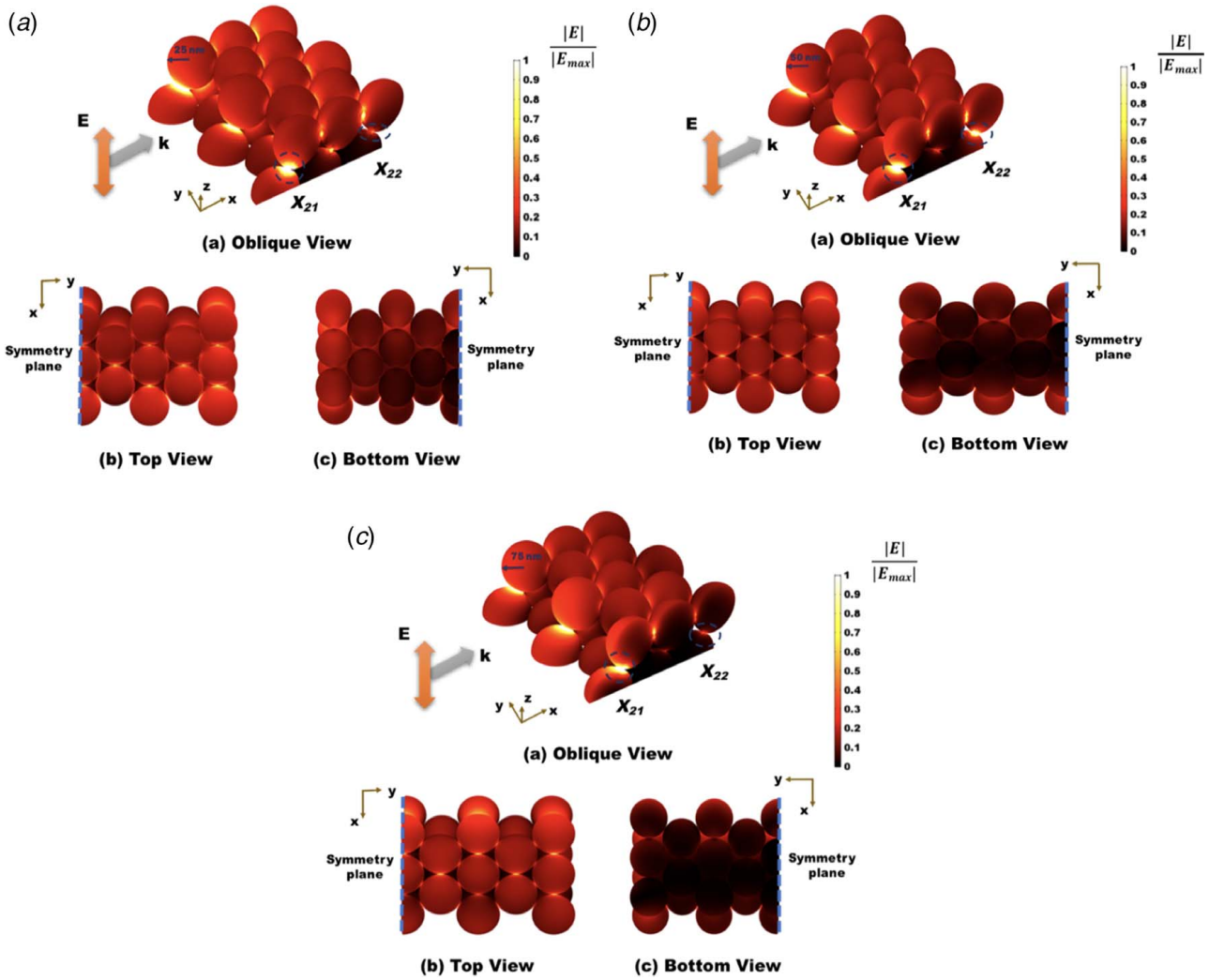

Fig. 8 Electric field distribution with $\lambda = 532$ nm, TM polarized light with varying radius for HCP configuration: (*a*) 25-nm radius, (*b*) 50-nm radius, and (*c*) 75-nm radius

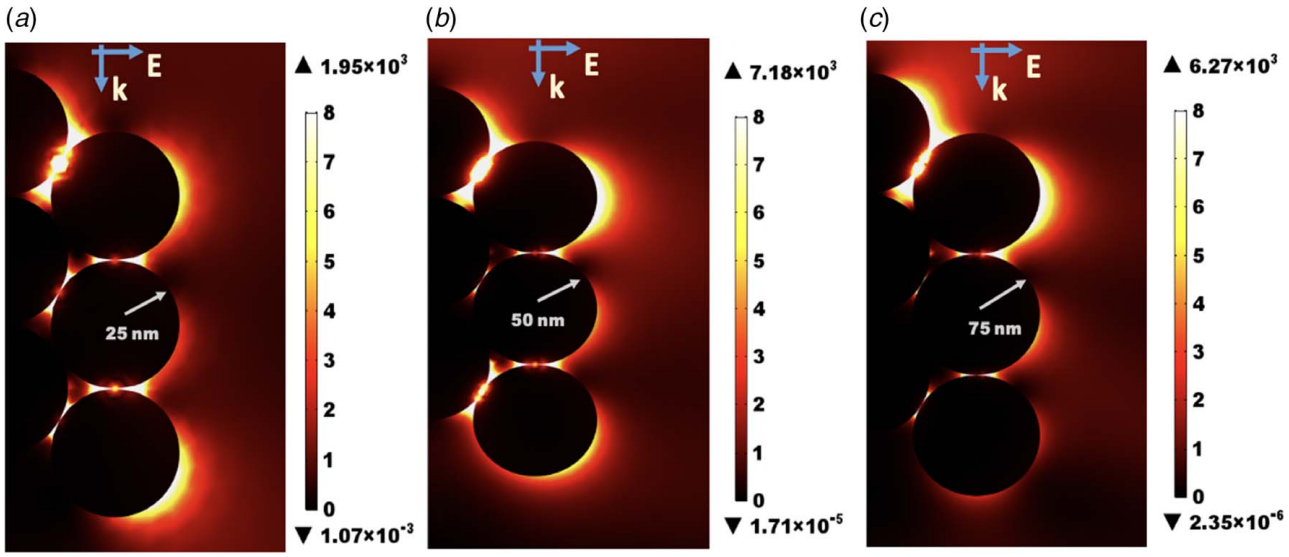

Fig. 9 Electric field intensity ($|I/I_0|$) with $\lambda = 532$ nm, TM polarized light with varying radius for HCP configuration at X_{21} and X_{22} cross section ($x-z$ plane at $y = 0$)

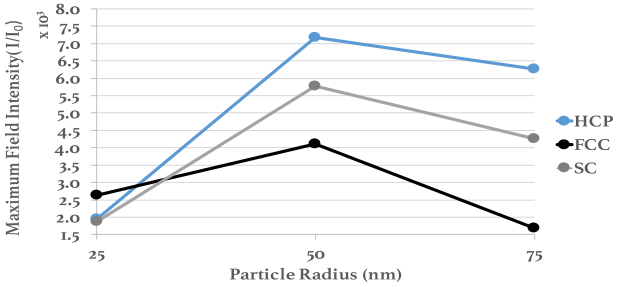

Fig. 10 Maximum field intensity ($|I/I_0|$) with $\lambda = 532$ nm, TM polarized light with varying radius for three configurations

domain. Because of the symmetry of the background field and the particle configurations, boundary conditions represent a mirror symmetry plane for the electric and magnetic fields. Hence, *xz* plane is defined as a perfect magnetic conductor (PMC) and *xy* plane as perfect electric conductor (PEC) at the symmetry planes for the simulated particle configurations, illustrated in Fig. 3(*b*). Also, we labeled the layer names as X_i where $i = 1,2,3$ to demonstrate the analyzed cross sections along the propagation direction for each particle configuration.

We analyze the scattering cross section by calculating the surface integration of the scattered Poynting vector over an imaginary surface enclosing all particles and located in the far-field ($kr >> 1$). Scattering efficiency is calculated as the ratio of scattering cross section to the surface area enclosing all particles. Absorption cross section is found by the volume integration of the absorbed energy within the nanoparticles, and absorption efficiency is obtained as the ratio of absorption cross section to the geometric cross section of the nanoparticle packings along the propagation direction. Also, single-scatter albedo (ω) is calculated as the ratio of scattering efficiency to the total extinction efficiency of the analyzed particle packings. Total resistive heating (W/m^3) in the nanoparticle packings is obtained by the analysis of the current density and stimulating electric field from the modeled symmetric geometries.

3 Results and Discussion

3.1 Near-Field Enhancement Between the Nanoparticles in Different Configurations. Figure 4 illustrates the electric field

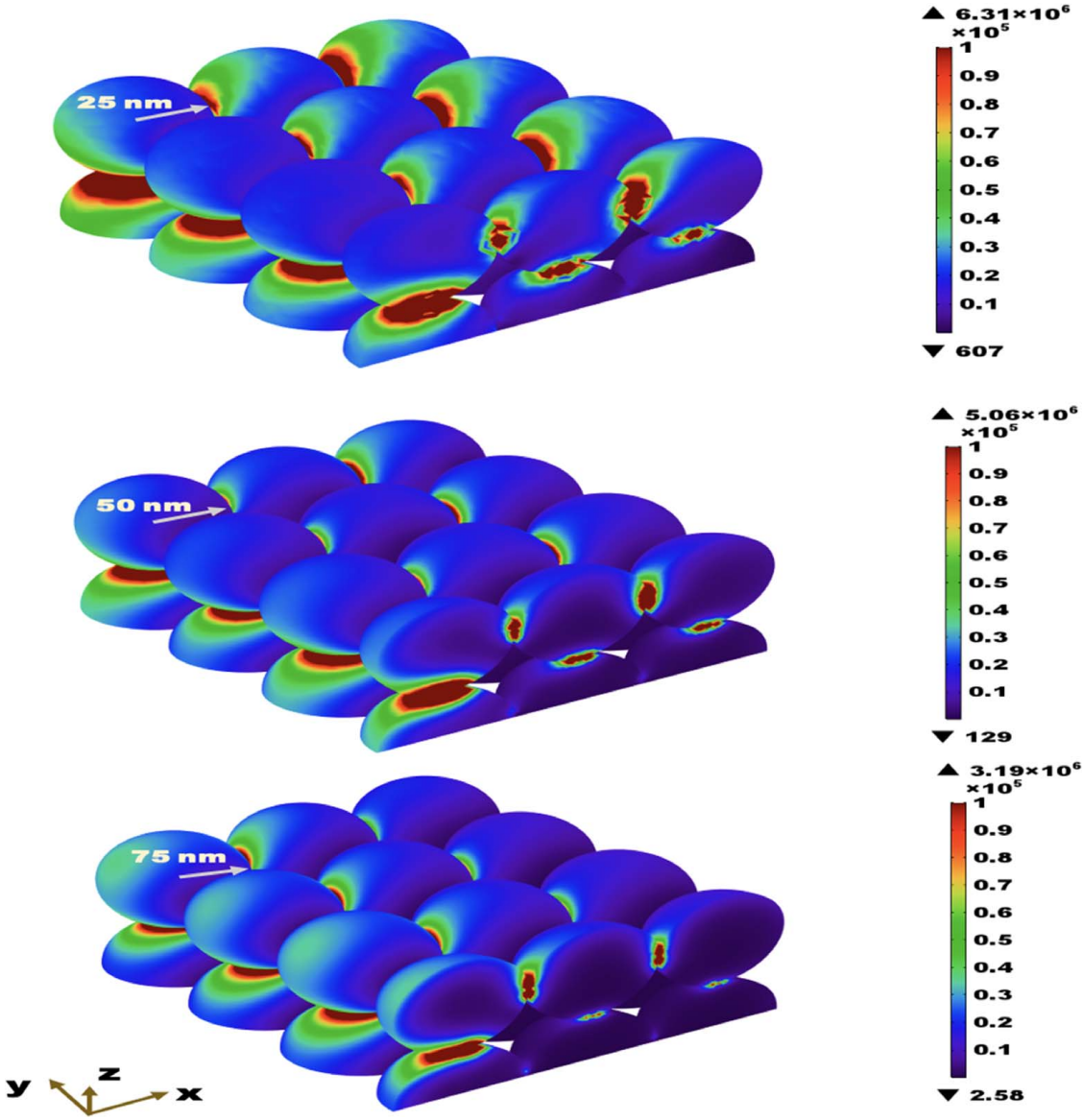

Fig. 11 Resistive heating (W/m^3) with $\lambda = 532$ nm, TM polarized light with varying radius for SC configuration

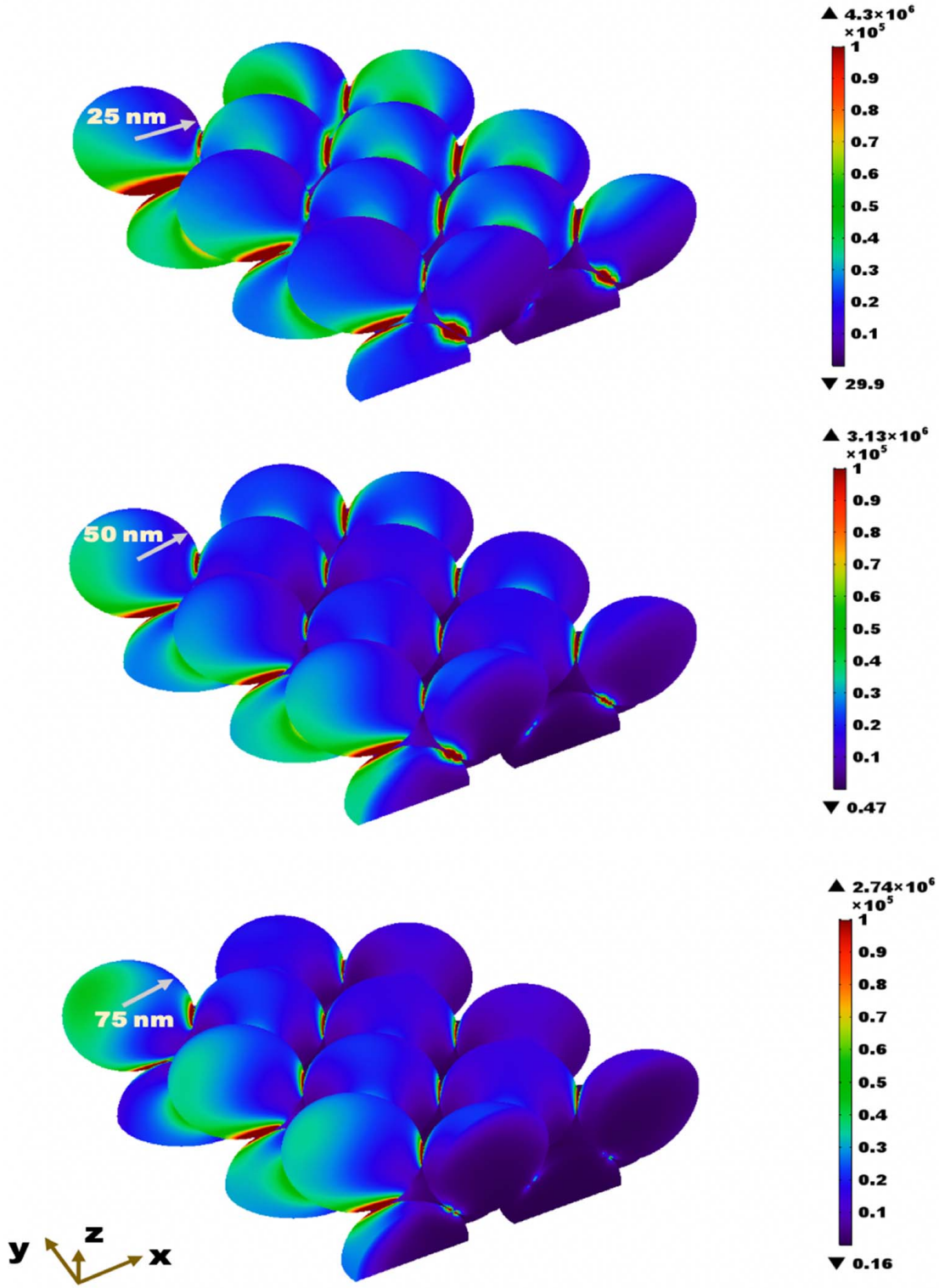

Fig. 12 Resistive heating (W/m^3) with $\lambda = 532$ nm, TM polarized light with varying radius for FCC configuration

enhancement with varying radius for SC configuration. We observed from bottom views that the propagation length of the light perpendicular to the propagation direction diminishes with increasing particle size due to radiation damping. The near-field confinement with respect to lattice plane is dependent on the line width of the collective resonance for nanoparticle chains [20]. This dependence implies that a broader collective resonance, which means a broader wavelength dependence, is achieved for smaller sizes of nanoparticles when the nanoparticles are packed into multilayers. This phenomenon is indeed observed for all other analyzed configurations.

Figure 5 shows that the maximum enhancement at the adjacent particles increases from 25 nm to 50 nm but then decreases from 50 nm to 75 nm. This suggests that 532-nm laser wavelength with TM polarization creates a plasmon resonance mode spanning the

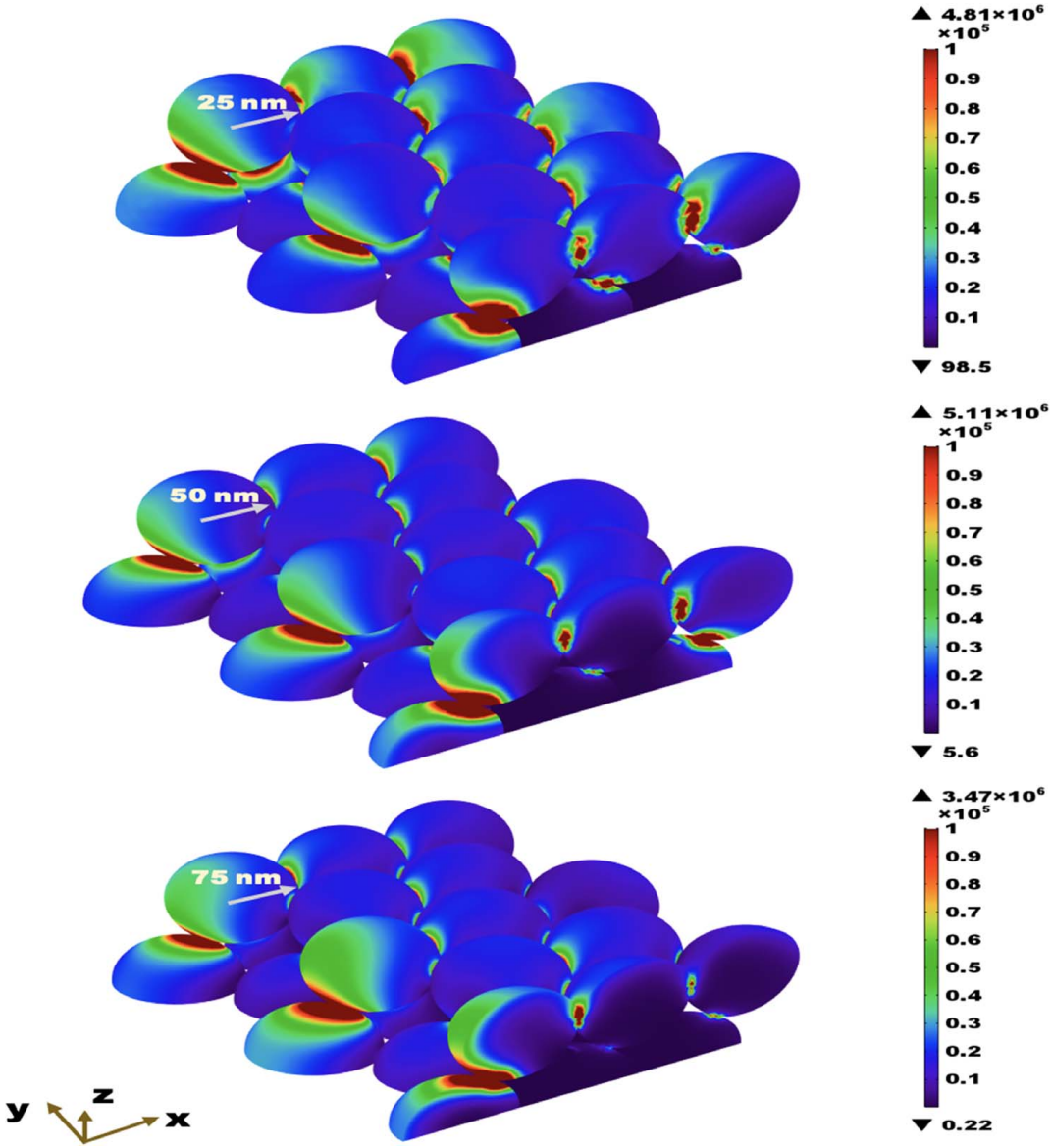

Fig. 13 Resistive heating (W/m^3) with $\lambda = 532$ nm, TM polarized light with varying radius for HCP configuration

interparticle gap for 50-nm radius in the SC configuration of copper nanoparticle packings. The presence of such a mode for radius 50 nm can lead to coherent near-field energy transport.

Figure 6 illustrates the electric field distribution with varying radius for FCC configuration. Figure 12 shows that the maximum enhancement at the adjacent particles first increases as the radius increases from 25 nm to 50 nm and then decreases with further increasing of the radius to 75 nm. We also observe that the near-field confinement width gets narrower when the particle radius increases from 25 nm to 75 nm. This can be explained as various multipoles radiation coupling and gap effect between the 75-nm radius particles for FCC configuration.

Also, the directions of the reflected and transmitted coupling mode might lead to destructive interference between the 75-nm radius particles which is also consistent with the result shown by Kujala et al. [21]. The coherency between the particles decreases as the particle size increases for FCC configuration under 532 nm, TM polarized light, due to the localization of the intensity between the adjacent particles, which can also be observed from Fig. 7.

Figure 8 illustrates the electric field distribution with varying radius for HCP configuration. We observe that the strongly coupled plasmon-polariton modes occur at a radius of 50 nm. This behavior is similar to that in the SC configuration because of the similarity of the particle arrangement. The only difference is due to the relative angle between the adjacent particles in SC configuration which results in different magnitudes of maximum electric field intensity for HCP configuration. This implies that the selected wavelength with the polarization direction creates a unique localized situation for adjacent particles with relative angle between the particles. We also observe that the near-field confinement width gets narrower and the polarization direction coupling reduces through the propagation direction when the particle radius further increases from 50 nm to 75 nm. Figure 9 also shows that the maximum enhancement at the adjacent particles increases from a particle radius increases of 25 nm to 50 nm but then decreases from 50 nm to 75 nm.

Overall, we observe that particle configuration does not strongly affect the resonant wavelength, but that the particle size does. We also observe that particle size and particle configuration affect the maximum electric field intensity in multilayer nanoparticle arrays and that a nonlinear thermo-optical response (as a function of particle radius) can be obtained from different configurations. SC,

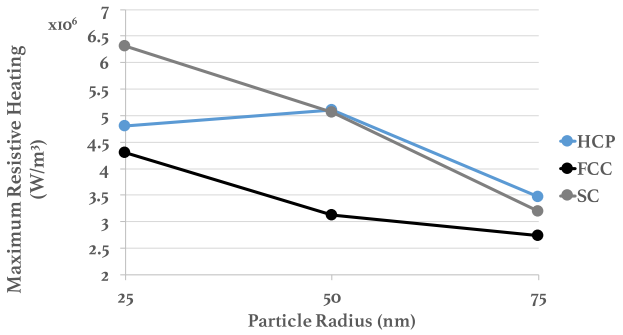

Fig. 14 Maximum resistive heating (W/m^3) with $\lambda = 532$ nm, TM polarized light with varying radius for three configurations

HCP, and FCC show similar trends in which the maximum electric field intensity is higher at a particle radius of 50 nm than at 25 nm, and yet lower at 75 nm than 50 nm. This shows that 532-nm wavelength creates a resonant mode for 50-nm radius of Cu nanoparticles. FCC has the highest maximum electric field intensity at small particle size (in our case 25 nm) and lowest electric field intensity at large particle size (in our case 75 nm). HCP exhibits the highest maximum electric field intensity at the resonant condition (when radius is at 50 nm). In addition, we see that maximum field intensity can be enhanced ~2-fold with particle size change when the particles are in the FCC configuration but can be increased ~3-fold in SC configuration and ~4-fold in HCP configuration as can be seen in Fig. 10. Therefore, the electric field enhancement is most sensitive to particle size when particles are arranged in the HCP configuration but least sensitive when the particles are arranged in the FCC configuration. Further studies need to be done to see how the enhancement sensitivity is affected by having non-monodisperse particles in the nanoparticle assemblies.

3.2 Resistive Heating Within the Nanoparticle Assemblies. Figure 11 shows the resistive heating (W/m^3) with varying radius for SC configuration. The maximum resistive heating occurs at 25-nm radius and is almost two times higher than for 75-nm radius. This trend is consistent with the decrease of absorption efficiency with particle size increase shown in Fig. 15(*a*).

Figure 12 illustrates the resistive heating with varying radius for FCC configuration. The maximum resistive heating occurs at 25-nm radius case and is almost 1.5 times higher than for 75-nm radius.

Another interesting result is that the absorption efficiency tends to be higher at 50-nm than 25-nm radius; however, maximum resistive heating is slightly lower at 50-nm than 25-nm radius. This

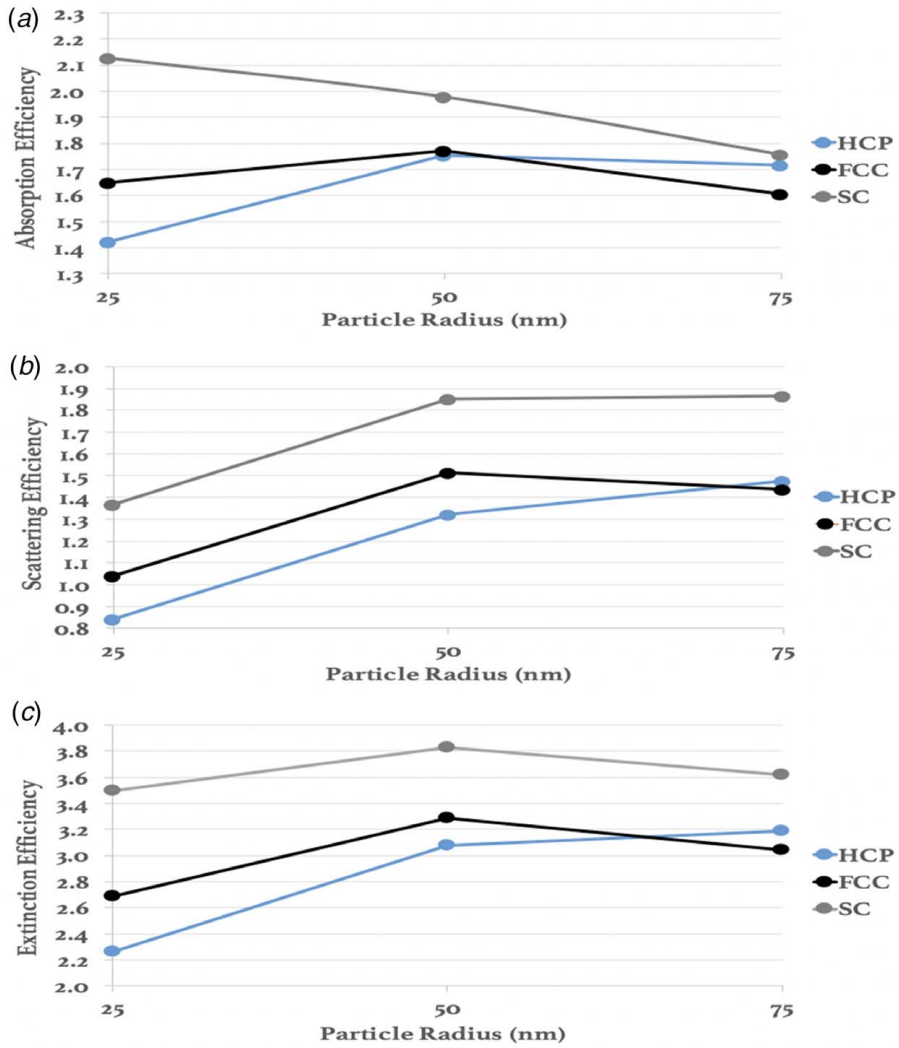

Fig. 15 Absorption, scattering, and extinction efficiency with varying radius (rad) for three configurations under $\lambda = 532$ nm, TM polarized light: (*a*) absorption efficiency, (*b*) scattering efficiency, and (c) extinction efficiency

might be caused by the particle size with gap modes that lead lower resistive losses due to the contact area or the effective geometrical area effect on absorption efficiency.

Figure 13 illustrates the resistive heating with varying radius for HCP configuration. It can be observed from Fig. 14 that the 50-nm radius case has the maximum resistive heating value out of the investigated 3 particle sizes and ~1.5 times higher than the 75-nm radius case. This trend is also consistent with the absorption efficiency which increases asymmetrically with the particle size increase.

Figure 14 summarizes the maximum resistive heating in different particle configurations for different particle size. It can be clearly seen that the resistive heating is higher for the smaller particle sizes. This could be due to the increased absorption in small particles relative to scattering with decreasing particle size. This decrease of scattering results in easier energy transport and increases the resistive heating when the particle size decreases. However, we observe for the specific case of the 50-nm radius nanoparticles in the HCP configuration that due to waveguide plasmon generation there is a slight increase in the resistive heating. We also note that resistive heating converges for all particle configurations as the particle radius becomes 75 nm.

3.3 Effect of Nanoparticle Size and Configuration on Absorption, Scattering, and Extinction Efficiency. The absorption efficiency is always the highest for all three particle sizes when the particles are arranged in the SC configuration (for 532 nm, TM illumination) as illustrated in Fig. 15(*a*). The absorption efficiencies of different particle configurations also converge when the particle radius increases, reaching values between ~1.6 and ~1.75 for 75-nm particle radius. The scattering efficiencies exhibit asymmetrical increase for all nanoparticle packings with different particle sizes due to Fano-type resonances [22].

Figure 15(*c*) shows the extinction efficiencies of the three different nanoparticle configurations. The total energy removed from the incident beam is the highest for SC configuration for all particle sizes. HCP has the lowest energy loss from the incident beam for 25-nm and 50-nm radius of particles; however, FCC has the lowest energy loss from the incident beam for 75-nm radius of particles. When the particle radius is larger than 50 nm, HCP and FCC configuration's behavior on extinction efficiency changes. This nonlinear trend might be caused by not decreasing the absorption efficiency significantly and high increase of the scattering efficiency for HCP configuration at a particle size larger than 50 nm (i.e., 75-nm radius) due to the collective modes between the adjacent particles. Another important point is that different particle arrangements significantly affect the attenuation and the trend of the extinction efficiency is also affected when the size of the particle is larger than 50 nm (i.e., 75-nm radius). Hence, the nonlinear thermo-optical response of the different nanoparticle configurations gives insight into penetration depth which then affects the depth of the sintering in the nanoparticle packings nonlinearly for different nanoparticle packing configurations with different particle sizes.

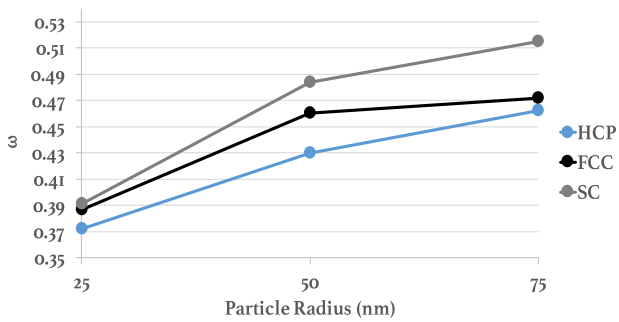

Fig. 16 A single-scatter albedo (ω) versus particle radius with $\lambda = 532$ nm, TM polarized light for three configurations

Figure 16 illustrates that as the particle radius increases from 25 nm to 75 nm, single-scatter albedo (ω) also increases for all nanoparticle configurations. This means that the photons interacting with the particles lead to more scattering than absorption in overall extinction when the particle size increases. Particle configuration does not affect significantly single scatter albedo for smaller size of particles (i.e 25-nm radius); however, this is not the case for larger particles and ω values start to diverge for different particle configurations at 75-nm radius. This also implies that the nanoparticle packings experience more absorption than scattering when packed with 25-nm radius nanoparticles in the overall extinction. Also, the HCP configuration has the lowest ω and SC configuration has the highest ω at all different sizes of particles between 25 nm to 75 nm.

4 Conclusion

We examine SC, FCC, and HCP nanoparticle packing configurations with monodisperse copper nanoparticles with radii of 25, 50, and 75 nm to understand the thermo-optical properties of the nanoparticle packings illuminated with 532-nm TM polarized light. Nonlinear thermal and optical responses are obtained for different particle configurations with different particle sizes, which affects the thermal energy transport in plasmon waveguides in the nanoparticle packings nonlinearly. Very high field intensity increases (more than ~7000-fold) can be obtained at 50-nm radius particle size with HCP nanoparticle configuration, and around 5800-fold field intensity increases with SC configuration due to interparticle plasmon resonance effects for these configurations. This implies that the relative angle between the adjacent particles in nanoparticle packings could lead to ~25% increase of the field intensity when the particles are packed densely in cluster form for 50 nm or larger particle sizes (i.e., 75-nm radius). Due to the gap between the particles in FCC nanoparticle packing, gap plasmon modes are very strong at 25-nm radius of particles which results in having much higher field intensity—up to ~30% higher than the SC and HCP configurations. Resistive heating is found to be highly dependent on the nanoparticle packing configuration and particle size. However, particle configuration starts to be less important in resistive heating for a larger particle size (i.e., 75-nm particle radius). Also, it is observed that as the particle radius increases from 25 nm to 75 nm, the single-scatter albedo (ω) also increases for all nanoparticle configurations. ω is highest for the SC configuration and lowest for the HCP configuration for all particle sizes from 25 nm to 75 nm, and ω begins to converge for all packing configurations as the particle radius increases to 75 nm. We note that at subnanometer length-scale, quantum effects have been observed and can cause deviations from the classical electromagnetics analysis of plasmons between the nanoparticles, due for example to electron tunneling and nonlocal screening [23,24]. The effects of electrical conductance and scattering at subnanometer length-scale, which could also affect thermo-optical properties and thermal energy transport, remain to be fully understood. New theoretical approaches and experimentation are needed to address subnanometer length-scale quantum effects fully. In this work, such effects are therefore not considered.

Overall, this study gives an insight into laser sintering of Cu nanoparticles and thermal energy transport between the nanoparticles for subwavelength 3D electronic interconnects. Based upon the modeling and the experimental observations, Cu nanoparticles should exhibit collective plasmon waveguides within different nanoparticle configurations when they are packed closely in cluster form and have a high potential for nanoscale plasmonic applications below the diffraction limit.

References

[1] Maier, S. A., Kik, P. G., Atwater, H. A., Meltzer, S., Harel, E., Koel, B. E., and Requicha, A. A., 2003, "Local Detection of Electromagnetic Energy Transport Below the Diffraction Limit in Metal Nanoparticle Plasmon Waveguides," Nat. Mater., **2**(4), pp. 229–232.

[2] Quinten, M., Leitner, A., Krenn, J. R., and Aussenegg, F. R., 1998, "Electromagnetic Energy Transport via Linear Chains of Silver Nanoparticles," Opt. Lett., **23**(17), pp. 1331–1333.
[3] Maqableh, M. M., Huang, X., Sung, S. Y., Reddy, K. S. M., Norby, G., Victora, R. H., and Stadler, B. J., 2012, "Low-Resistivity 10 nm Diameter Magnetic Sensors," Nano Lett., **12**(8), pp. 4102–4109.
[4] Josell, D., Brongersma, S. H., and Tőkei, Z., 2009, "Size-Dependent Resistivity in Nanoscale Interconnects," Annu. Rev. Mater. Res., **39**(1), pp. 231–254.
[5] Kreibig, U., and Vollmer, M., 2013, *Optical Properties of Metal Clusters*, Vol. Vol. 25, Springer Science & Business Media, Berlin/Heidelberg.
[6] Jensen, T. R., Duval, M. L., Kelly, K. L., Lazarides, A. A., Schatz, G. C., and Van Duyne, R. P., 1999, "Nanosphere Lithography: Effect of the External Dielectric Medium on the Surface Plasmon Resonance Spectrum of a Periodic Array of Silver Nanoparticles," J. Phys. Chem. B, **103**(45), pp. 9846–9853.
[7] Tsang, T. Y., 1996, "Surface-Plasmon-Enhanced Third-Harmonic Generation in Thin Silver Films," Opt. Lett., **21**(4), pp. 245–247.
[8] Félidj, N., Aubard, J., Lévi, G., Krenn, J. R., Salerno, M., Schider, G., Lamprecht, B., Leitner, A., and Aussenegg, F. R., 2002, "Controlling the Optical Response of Regular Arrays of Gold Particles for Surface-Enhanced Raman Scattering," Phys. Rev. B, **65**(7), p. 075419.
[9] Stockman, M. I., Bergman, D. J., Anceau, C., Brasselet, S., and Zyss, J., 2004, "Enhanced Second-Harmonic Generation by Metal Surfaces With Nanoscale Roughness: Nanoscale Dephasing, Depolarization, and Correlations," Phys. Rev. Lett., **92**(5), p. 057402.
[10] Lamprecht, B., Leitner, A., and Aussenegg, F. R., 1999, "SHG Studies of Plasmon Dephasing in Nanoparticles," Appl. Phys. B: Lasers Opt., **68**(3), pp. 419–423.
[11] Canfield, B. K., Kujala, S., Jefimovs, K., Turunen, J., and Kauranen, M., 2004, "Linear and Nonlinear Optical Responses Influenced by Broken Symmetry in an Array of Gold Nanoparticles," Opt. Exp., **12**(22), pp. 5418–5423.
[12] Jin, R., Jureller, J. E., and Scherer, N. F., 2006, "Precise Localization and Correlation of Single Nanoparticle Optical Responses and Morphology," Appl. Phys. Lett., **88**(26), p. 263111.
[13] Yuksel, A., and Cullinan, M., 2016, "Modeling of Nanoparticle Agglomeration and Powder Bed Formation in Microscale Selective Laser Sintering Systems," Addit. Manuf., **12**(Part B), pp. 204–215.
[14] Harvey, A., Backes, C., Boland, J. B., He, X., Griffin, A., Szydlowska, B., Gabbett, C., Donegan, J. F., and Coleman, J. N., 2018, "Non-resonant Light Scattering in Dispersions of 2D Nanosheets," Nat. Commun., **9**(1), pp. 1–11.
[15] Fan, X., Zheng, W., and Singh, D. J., 2014, "Light Scattering and Surface Plasmons on Small Spherical Particles," Light: Sci. Appl., **3**(6), pp. e179–e179.
[16] Guerra, L. F., Muir, T. W., and Yang, H., 2019, "Single-Particle Dynamic Light Scattering: Shapes of Individual Nanoparticles," Nano Lett., **19**(8), pp. 5530–5536.
[17] Bosbach, J., Martin, D., Stietz, F., Wenzel, T., and Träger, F., 1999, "Laser-Based Method for Fabricating Monodisperse Metallic Nanoparticles," Appl. Phys. Lett., **74**(18), pp. 2605–2607.
[18] Yuksel, A., Yu, E. T., Murthy, J., and Cullinan, M., 2017, "Effect of Substrate and Nanoparticle Spacing on Plasmonic Enhancement in Three-Dimensional Nanoparticle Structures," J. Micro Nano Manuf., **5**(4), p. 040903.
[19] Johnson, P. B., and Christy, R. W., 1972, "Optical Constants of the Noble Metals," Phys. Rev. B, **6**(12), pp. 4370–4379.
[20] Evlyukhin, A. B., Reinhardt, C., Zywietz, U., and Chichkov, B. N., 2012, "Collective Resonances in Metal Nanoparticle Arrays With Dipole-Quadrupole Interactions," Phys. Rev. B, **85**(24), p. 245411.
[21] Kujala, S., Canfield, B. K., Kauranen, M., Svirko, Y., and Turunen, J., 2007, "Multipole Interference in the Second-Harmonic Optical Radiation From Gold Nanoparticles," Phys. Rev. Lett., **98**(16), p. 167403.
[22] Luk'yanchuk, B., Zheludev, N. I., Maier, S. A., Halas, N. J., Nordlander, P., Giessen, H., and Chong, C. T., 2010, "The Fano Resonance in Plasmonic Nanostructures and Metamaterials," Nat. Mater., **9**(9), pp. 707–715.
[23] Ciracì, C., Hill, R. T., Mock, J. J., Urzhumov, Y., Fernández-Domínguez, A. I., Maier, S. A., Pendry, J. B., Chilkoti, A., and Smith, D. R., 2012, "Probing the Ultimate Limits of Plasmonic Enhancement," Science, **337**(6098), pp. 1072–1074.
[24] Zhu, W., Esteban, R., Borisov, A. G., Baumberg, J. J., Nordlander, P., Lezec, H. J., Aizpurua, J., and Crozier, K. B., 2016, "Quantum Mechanical Effects in Plasmonic Structures With Subnanometre Gaps," Nat. Commun., **7**(1), pp. 1–14.